Interferometric test for N-wave flow

By D. H. STEININGER and F. D. BENNETT
Ballistic Research Laboratories, Aberdeen Proving Ground, Maryland

(*Received* 8 *December* 1956)

SUMMARY

An analytical expression for the fringe shift in the N-wave is derived from the improved linearized theory for a slender supersonic projectile. From this expression an approximate mapping function is found which gives a simple test for N-wave flow. The validity of the fringe-shift expression is quantitatively confirmed by measuring an interferogram of the flow around a sphere. N-wave flow is shown to exist around a small sphere for r greater than about 70 diameters. Measurements of the shock waves from a sphere and a cone-cylinder show that the shocks assume their asymptotic positions for $r > 14$ diameters for the sphere, and $r > 7$ diameters for the cone-cylinder.

1. INTRODUCTION

1.1. *Interferometric method of analysis*

Interferometric investigation of the fluid flow around a supersonic projectile in free flight gives a quantitative record of the density over the entire flow field (Ladenburg & Bershader 1954). Experience shows that the reduction of the fringe shift to density values for an axisymmetric flow is a cumbersome and time-consuming process because, in general, the relationship between fringe shift and density at a particular point is not simple. It is useful, therefore, to find flow regions for which some intrinsic property can be determined directly from the measurements of fringe shift.

An interferogram of a supersonic cone-cylinder shows two regions which have conspicuous symmetry of fringe shape, suggesting the possibility of a simplified analysis. The first of these is the region near the cone in which the fringes are nearly straight and parallel (Giese, Bennett & Bergdolt 1950; Giese & Bergdolt 1953; Bergdolt 1953; Cole, Solomon & Willmarth 1953). The flow here is characterized by the fact that the physical variables are constant along straight lines through the vertex. Assumption of this flow regularity leads to a method of plotting fringe shift which verifies in many instances the approximation of real flows to idealized conical flow.

The second of these regions lies between the front and rear shock waves at rather large distances from the projectile axis. Here the fringes have a gentle curvature and a similarity of shape which change only slowly as the

distance from the axis increases. This similarity suggests an underlying simplicity of the fundamental flow field. Experiments by DuMond *et al.* (1946) showed that at large radial distances, the pressure profile parallel to the axis consists of a sudden rise at the front shock, followed by a linear decrease to a value below that for the free stream, and then a sudden rise at the rear shock. The curve so generated has the shape of a capital N; hence is given the name 'N-wave'.

1.2. *Scope of the paper*

Using the results obtained by Whitham (1952) in his improved linearized theory for slender supersonic projectiles, we derive here an analytical expression for the fringe shift in the N-wave region. We investigate this function and find a mapping property which gives a simple criterion for comparing theoretical and measured data.

Interferograms taken of the flow around spheres and slender cone-cylinders are measured, and observed fringe shift is compared with the theory. To justify the use of spheres, we discuss the validity of comparing the distant flow around blunt bodies with values predicted by slender-body theory. Figure 1 (plate 1) shows a general view of the flow about a sphere.

2. Theory

2.1. *The fringe-shift integral*

If (x, r) are the cylindrical polar coordinates of the axisymmetric disturbance, and the front tip of the projectile is at the origin with the line of flight parallel to the x-axis, then the fringe shift $\delta(x, r)$ is related (Bennett *et al.* 1952) to the density ρ at (x, r) by

$$\delta(x, r) = \frac{2K}{\lambda} \int_r^{r_N} \frac{(\rho - \rho_0) t \, dt}{(t^2 - r^2)^{1/2}}, \tag{2.1}$$

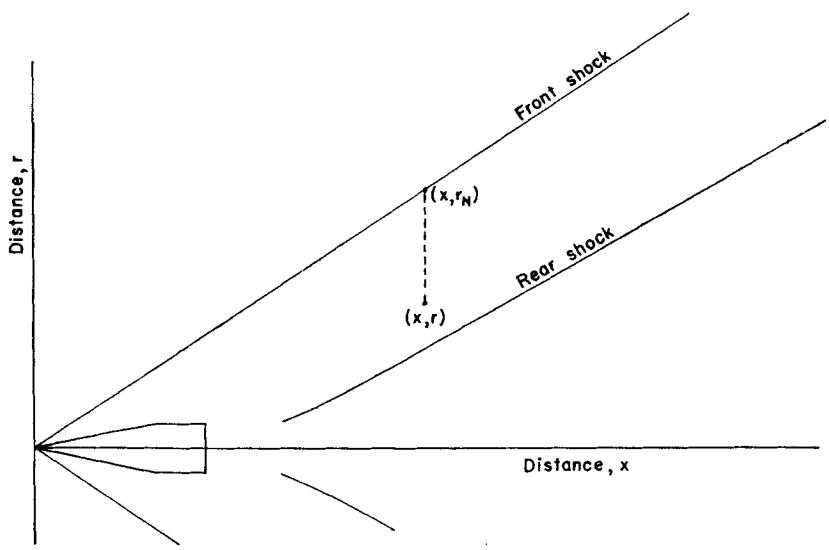

Figure 2. Path of integration of the fringe-shift integral for a supersonic projectile.

where K is the Gladstone–Dale constant, λ the wavelength of the light in vacuum, ρ_0 the free-stream density, r_N the outer radius of the disturbance at x, and t is the variable of integration in the r direction. As in figure 2, the fringe shift at (x, r) is determined by an integration of the density values found along the line from r to r_N.

An inversion of (2.1) allows the reduction of fringe-shift measurements to density throughout the flow field. Such a reduction does not interest us here; for our purpose is to obtain in the N-wave a functional description of $(\rho - \rho_0)$ and from it derive an expression for the fringe shift in that region.

2.2. *Improved linearized theory*

The linearized theory of Karman & Moore (1932) for a slender supersonic projectile gives solutions which are good first approximations to the actual conditions at the surface of the projectile, but which fail as the distance r increases. This failure arises from the fact that the Mach lines are parabolae in a second approximation, while the linear approximations to them are straight lines; and although a curved Mach line intersects a straight one at the surface of the body, the curves diverge with increasing r. The improved theory offered by Whitham (1952) makes the linear solutions uniformly valid over the entire field by associating them with the more exact Mach lines. This improved theory is still based upon a first approximation to the potential flow equations, and, like linear theory, neglects terms of order u^2, v^2, where u and v are the small perturbation velocities in the x and r directions. Nevertheless, it has the additional advantage over linear theory that the existence and position of the shock waves are predicted.

With this background in mind, we now discuss that part of the Whitham theory necessary to our development. Equations which appear in Whitham's paper are identified by the notation *Wh*.

1. *The shock waves.* At great distances from its axis, the supersonic projectile produces two shock waves, both extending to infinity. The equations for the shock waves at large r are, from *Wh*(43),

$$x = \alpha r + y_0 \mp A r^{1/4}, \tag{2.2}$$

where the upper sign represents the front shock and the lower sign the rear shock, $\alpha^2 = M^2 - 1$, and A and y_0 are constants related to body shape. The straight line $x = \alpha r + y_0$ and the lines given by (2.2) intersect the x-axis at y_0. By inspection of (2.2) one sees that the front shock wave lies ahead, and the rear shock behind the straight line by the amount $Ar^{1/4}$. Thus, the horizontal distance between the two shocks is $2Ar^{1/4}$. This property will be used later to determine A experimentally. The fact that the locus of the mid-points of the horizontal distances is the line $x = \alpha r + y_0$ will enable us to determine α when the projectile axis is known, or the projectile axis when α is known.

2. *The pressure distribution.* When r is large, the pressure distribution between the shock waves is by *Wh*(71),

$$(p - p_0)/p_0 = \gamma M^2 (2\alpha)^{-1/2} (kr)^{-1} (\alpha r - x + y_0) \tag{2.3}$$

where $k = 2^{-1/2}(\gamma+1)M^4\alpha^{-3/2}$, p is the disturbed and p_0 the free-stream pressure. Notice that along a trace of constant r the pressure difference $p-p_0$ decreases linearly with x from a positive value at the front shock to an equal negative value at the rear shock. Midway between the shocks on the straight characteristic, we have $p = p_0$. The pressure slope, $\gamma M^2(kr)^{-1}(2\alpha)^{-1/2}$ depends only on the flow constants and the distance from the axis, and not upon the shape of the body producing the disturbance. In addition to this expression for the N-wave distribution, which only exists in the distant regions, Whitham derives a more general equation which gives the pressure distribution at any distance from the projectile axis. Figure 3 shows a typical pressure signature along a horizontal trace for three distances from the axis:—near to the body and before the rear shock is formed, an intermediate position with both shocks, and the final wave.

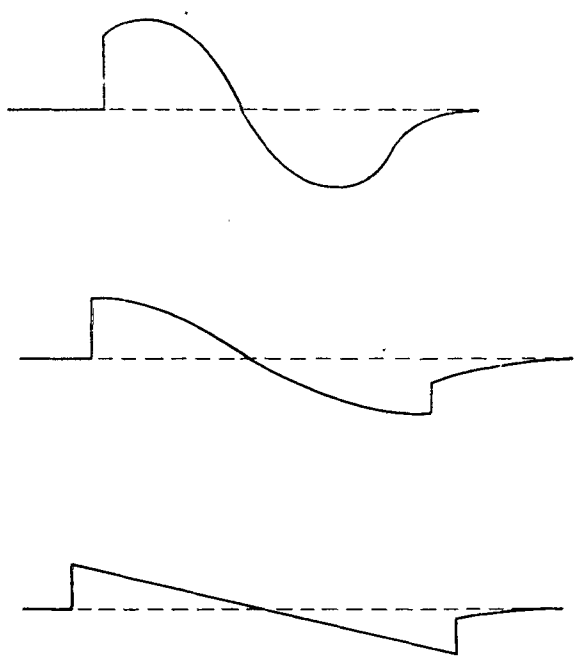

Figure 3. Typical pressure signatures along horizontal traces: top curve, near the body; middle curve, at an intermediate distance; bottom curve, in the N-wave region.

2.3. *Density distribution in the N-wave*

We now relate pressure and density in the N-wave. Despite the seeming simplicity of this programme, some care must be exercised to assure an approximation consistent with that of linearized theory.

It can be shown (Heaslet & Lomax 1954) that the entropy may be considered constant across a shock wave if third and higher-order powers

of the perturbation velocities are neglected. We neglect second and higher-powers and may, therefore, assume that the flow behind the shock is isentropic. The adiabatic gas law applies; thus

$$\rho/\rho_0 = (p/p_0)^{1/\gamma}. \tag{2.4}$$

Expanding (2.4) in Taylor series around $p = p_0$, we get

$$\left(\frac{p}{p_0}\right)^{1/\gamma} = 1 + \frac{1}{\gamma}\left(\frac{p-p_0}{p_0}\right) + \frac{1-\gamma}{2\gamma^2}\left(\frac{p-p_0}{p_0}\right)^2 + O\left(\frac{p-p_0}{p_0}\right)^3.$$

In *Wh*(66), Whitham finds that

$$(p-p_0)/p_0 = O(u);$$

so to the linear approximation

$$\frac{\rho}{\rho_0} = \left(\frac{p}{p_0}\right)^{1/\gamma} = 1 + \frac{1}{\gamma}\left(\frac{p-p_0}{p_0}\right),$$

and

$$\frac{\rho-\rho_0}{\rho_0} = \frac{1}{\gamma}\left(\frac{p-p_0}{p_0}\right). \tag{2.5}$$

If we substitute (2.3) into (2.5), we find that

$$\rho-\rho_0 = \rho_0 M^2 k^{-1}(2\alpha)^{-1/2} r^{-1}(\alpha r - x + y_0). \tag{2.6}$$

This is the density distribution between the shock waves in the N-wave region. Along a trace of constant r, the density profile of the N-wave has the same characteristic shape as the pressure curve.

2.4. *Fringe shift between the shock waves*

Combining (2.6) and (2.1), we obtain

$$\delta(x,r) = \frac{\sqrt{2}K\rho_0 M^2}{\lambda k \alpha^{1/2}} \int_r^{r_N} \frac{(\alpha t - x + y_0)}{(t^2-r^2)^{1/2}}\, dt. \tag{2.7}$$

Here x is constant along the path of integration from r to r_N. Regrouping terms and integrating, we find

$$\delta(x,r) = \frac{K\rho_0 M^2 (2\alpha)^{1/2} r}{\lambda k} \times$$
$$\times \left\{\left[\left(\frac{r_N}{r}\right)^2 - 1\right]^{1/2} - \left(\frac{x-y_0}{\alpha r}\right)\log\left[\frac{r_N}{r} + \left(\frac{r_N^2}{r^2} - 1\right)^{1/2}\right]\right\}, \tag{2.8}$$

where r_N is related to x by means of the front shock equation

$$x = \alpha r_N + y_0 - A r_N^{1/4}. \tag{2.9}$$

Equations (2.8) and (2.9) predict the fringe shift between the shock waves.

Let us examine the variation of $\delta(x,r)$ along a trace $r =$ const. as x increases from x_N to x_S, which lie on the front and rear shocks respectively. Also, x_0 lies on the line $x - \alpha r = y_0$, halfway between x_N and x_S (see figure 4).

Let $f(\epsilon) = (\epsilon^2-1)^{1/2}$, $g(\epsilon) = \log[\epsilon+(\epsilon^2-1)^{1/2}]$, and $R = (x-y_0)/\alpha r$, where $\epsilon = r_N/r$. For a particular flow the magnitude and sign of δ is determined from (2.8) by the term in the curly brackets, i.e. by $\{f-Rg\}$.

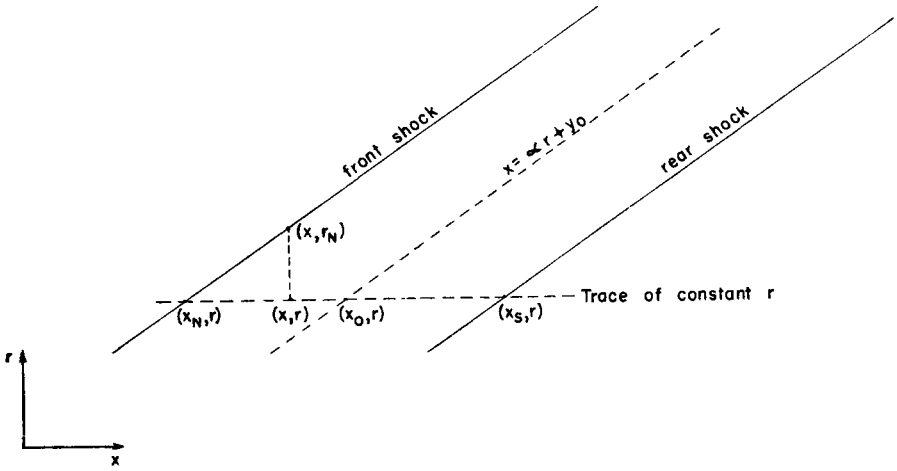

Figure 4. The region between the two shock waves.

By comparison with the equation of the straight characteristic

$$R \begin{Bmatrix} <1 \\ =1 \\ >1 \end{Bmatrix} \quad \text{if} \quad \begin{Bmatrix} x < x_0, \\ x = x_0, \\ x > x_0. \end{Bmatrix}$$

Thus R increases monotonically with x from a value less than 1 at the front shock to a value greater than 1 at the rear shock. From the equation of the front shock wave,

$$1-(A/\alpha)r^{-3/4} \leqslant R \leqslant 1+(A/\alpha)r^{-3/4}.$$

The variation of $f(\epsilon)$ and $Rg(\epsilon)$ with ϵ is shown in figure 5 for $R \leqslant 1$. The curves have vertical tangents at $\epsilon = 1$ and intersect at no other point. (A proof of this fact appears in Appendix I.) When $R > 1$, they are related as in figure 6. In addition to their intersection and common vertical tangent at $\epsilon = 1$, they intersect at one other point, say $\epsilon = \epsilon_c$ (see Appendix I), where ϵ_c increases as R increases.

We can now examine the combination of functions $\{f-Rg\}$. As x increases, so do ϵ, R, and ϵ_c (when $R > 1$).

When $x_N \leqslant x \leqslant x_0$, $R \leqslant 1$, so $f > Rg$. Therefore, δ is positive in the forward portion of the N-wave.

When $x_0 < x \leqslant x_S$, $R > 1$, and $f \gtreqless Rg$ if $\epsilon \gtreqless \epsilon_c$. When x is just greater than x_0, $\epsilon > \epsilon_c$, so δ is positive. But it is possible that as x increases, ϵ_c increases faster than ϵ. If it does, then the conditions $\epsilon \leqslant \epsilon_c$ can occur, and δ will pass through zero to negative values near the rear shock wave. The proof that $\partial\epsilon_c/\partial x > \partial\epsilon/\partial x$ is too complicated to be attempted here. We resort to calculation to establish the behaviour of δ in this region.

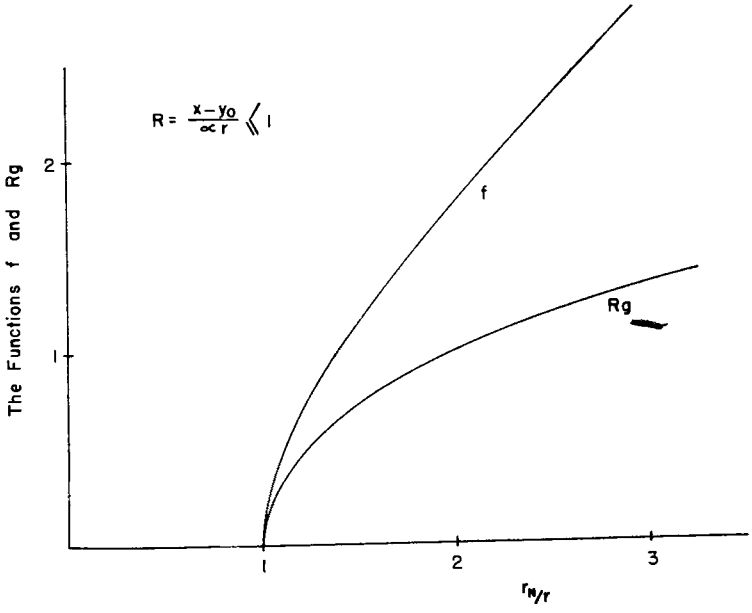

Figure 5. Variation of the functions f and Rg when $R \leqslant 1$.

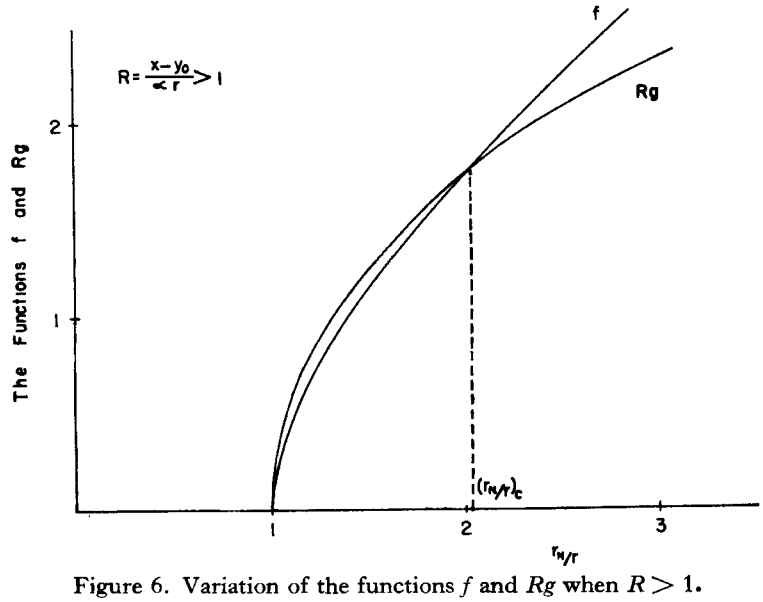

Figure 6. Variation of the functions f and Rg when $R > 1$.

A calculation of δ *vs* x along r = const. from (2.8), using representative values of A, y_0 and the flow constants, yields the curve in figure 7. The fringe shift does go to negative values near the rear shock wave.

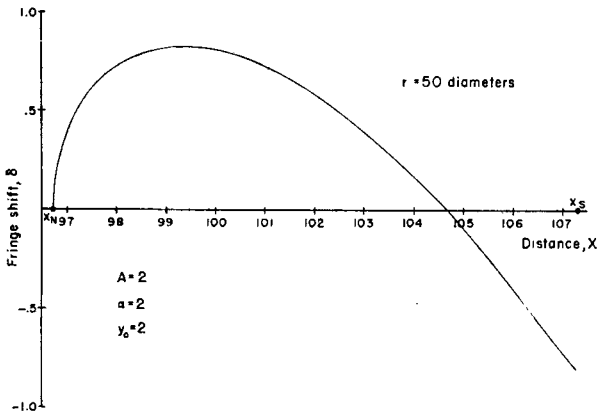

Figure 7. Variation of fringe shift along a horizontal trace, calculated from (2·8).

2.5. *Fringe-shift mapping law*

Let us investigate the behaviour of the δ *vs* x curve of figure 7 at several radial distances. Table 1 gives the calculated values of δ along three horizontal traces. Preliminary calculations* of δ *vs* x show that δ becomes zero about three-quarters of the way between x_N and x_S, no matter what the value of r. This indicates that the ratio $(x-x_N)/(x_S-x_N)$ has a significance which is independent of r; so in table 1, δ is given for values of

$$\xi = (x-x_N)/(x_S-x_N), \qquad \text{Definition 1} \quad (2.10)$$

rather than for values of x. Theoretically, $x_S - x_N = 2Ar^{1/4}$ by (2.2), and so

$$\xi = (x-x_N)/2Ar^{1/4}. \qquad \text{Definition 2} \quad (2.11)$$

Between the shock waves, $0 \leqslant \xi \leqslant 1$. The variable ξ seems indeed to be independent of r in that all the curves of δ *vs* ξ given in table 1 pass through zero and reach positive maxima for the same values of ξ. However, the magnitude of δ decreases as r increases.

Because of the inverse variation of δ with r, it seemed possible that for any two traces the relation $\delta_1 r_1^n = \delta_2 r_2^n$ might hold for each value of ξ along the traces. When values of δ and r were substituted in this equation, n turned out to be very close to $\frac{1}{8}$. For each trace, then, the values of δ were multiplied by $r^{1/8}$. A plot of $\delta r^{1/8}$ *vs* ξ yields a curve which remains closely the same for all horizontal traces through the N-wave. Comparison

* A discussion of this investigation is being published in an Office of Ordnance Research Report on the Second Annual Conference of Ordnance Mathematicians, February 1956. Inquiries should be addressed to Office of Ordnance Research, Box CM, Duke Station, Durham, North Carolina.

of the last three columns of table 1 shows the agreement possible. The last two columns agree to better than 1% for many of the entries. The variables ξ and δ are dimensionless; values of the coordinates are rendered dimensionless by dividing them by the projectile diameter.

ξ	δ			$\delta r^{1/8}$		
	$r = 10$	$r = 50$	$r = 100$	$r = 10$	$r = 50$	$r = 100$
0	0	0	0	0	0	0
0·1	0·840 2	0·676	0·618	1·120 4	1·102	1·099
0·2	1·004 8	0·808	0·740	1·339 9	1·318	1·316
0·3	1·009 0	0·812	0·742	1·345 5	1·324	1·320
0·4	0·909 4	0·731	0·666	1·212 7	1·192	1·184
0·5	0·732 0	0·585	0·534	0·976 1	0·954	0·950
0·6	0·490 6	0·385	0·350	0·654 2	0·628	0·622
0·7	0·196 6	0·145	0·130	0·262 2	0·237	0·231
0·8	−0·146 6	−0·138	−0·130	−0·195 5	−0·225	−0·231
0·9	−0·513 6	−0·455	−0·422	−0·708 9	−0·742	−0·750
1·0	−0·955 6	−0·807	−0·742	−1·274 3	−1·316	−1·320

Table 1. Fringe shift calculated from equation (2·8); flow constants are $A = 2$, $\alpha = 2$, $y_0 = 2$.

We now show that the $\delta r^{1/8}$ mapping law is contained implicitly in the exact N-wave fringe-shift equation (2.8), and can be revealed by making uitable approximations.

Referring to § 2.4 and making use of the definitions given there, we can write (2.8) as

$$\delta = Cr\{f - Rg\}; \tag{2.12}$$

where $C = (2\alpha)^{1/2} K\rho_0 M^2(\lambda k)^{-1}$, and f, g are functions only of ϵ $(= r_N/r)$. Further, let $(A/\alpha)r^{-3/4} = \sigma$, and observe that σ is proportional to Whitham's approximate expression for the shock strength, *Wh*(44). Our task is now to find R, f and g as functions of σ and ξ. For R this is comparatively easy and leads to a general proof of the possibility for f and g.

The geometric relationship between an external point (x, r) and the corresponding points on the front shock wave (x_N, r) and (x, r_N) is made clear schematically in figure 4. Selecting the minus sign in (2.2), we may write

$$x_N = \alpha r + y_0 - Ar^{1/4}, \tag{2.13 a}$$

and

$$x = \alpha r_N + y_0 - Ar_N^{1/4}. \tag{2.13 b}$$

Substituting (2.13 a) into (2.11), the definition of ξ, we obtain

$$\xi = (x - \alpha r - y_0 + Ar^{1/4})/2Ar^{1/4},$$

and solving this for $(x - y_0)/\alpha r$ gives

$$R = 1 - \sigma + 2\sigma\xi. \tag{2.14}$$

Division of (2.13 b) by αr yields a relation between ϵ, σ and R as follows:

$$\epsilon - \sigma\epsilon^{1/4} - R = 0. \tag{2.15}$$

From the quartic equation (2.15), it is clear that $\epsilon = \epsilon(\sigma, R)$. From (2.14) it follows that ϵ is a function only of σ and ξ; consequently, the same is true of f and g. It remains now to find suitable expressions for these two functions.

As a preliminary step, we find bounds for ϵ. From the definition it is clear that $1 \leqslant \epsilon \leqslant r_N/r_S$. The shock-wave equations (2.2) evaluated at x yield

$$\alpha r_N - Ar^{1/4} = \alpha r_S + Ar_S^{1/4},$$

or upon dividing by αr_S,

$$(r_N/r_S) - 1 = \sigma_S[(r_N/r_S)^{1/4} + 1], \tag{2.16}$$

where $\sigma_S = (A/\alpha)r_S^{-3/4}$. As $r \to \infty$, the shock strength σ_S approaches zero, and it follows from (2.16) that $r_N/r_S \to 1$. By choosing r_S sufficiently large, we can bring ϵ as close to unity as we please. We may therefore set $\epsilon = 1 + \nu$, where $\nu = \nu(r_S) \ll 1$ is as small as we please.

The quantity ν may now be evaluated by approximating the solution of the quartic (2.15). Saving terms up to $O(\nu^2)$ in the binomial expansion of $\epsilon^{1/4}$, we find

$$\nu = \{R - 1 + \sigma[1 + O(\nu^2)]\}(1 - \tfrac{1}{4}\sigma)^{-1}. \tag{2.17}$$

With (2.14) this becomes

$$\nu = 2\sigma\xi(1 - \tfrac{1}{4}\sigma)^{-1} + O(\sigma\nu^2). \tag{2.17 a}$$

Equation (2.17 a) shows that ν is of the order $\sigma\xi$. By (2.10) or (2.11) it is clear that $\xi = O(1)$; hence we conclude that ν is $O(\sigma)$. Upon saving terms of order σ^2 in (2.17 a), we have

$$\nu = 2\sigma\xi(1 + \tfrac{1}{4}\sigma) + O(\nu^3). \tag{2.18}$$

By definition, $f = (\epsilon^2 - 1)^{1/2} = (2\nu + \nu^2)^{1/2}$. Using (2.18) and expanding the square root, we find that

$$f = 2(\sigma\xi)^{1/2}[1 + \tfrac{1}{8}\sigma + \tfrac{1}{2}\sigma\xi + O(\sigma^2)]. \tag{2.19}$$

A suitable expression for g is slightly more difficult to get. We proceed as follows. Solve $f = (\epsilon^2 - 1)^{1/2}$ for ϵ, and obtain $\epsilon = (f^2 + 1)^{1/2}$. Then

$$g = \log[\epsilon + (\epsilon^2 - 1)^{1/2}] = \log[f + (f^2 + 1)^{1/2}]. \tag{2.20}$$

The expansion for (2.20) may be obtained in the form

$$g = \sum_1^\infty b_n f^{2n-1}, \tag{2.21 a}$$

where

$$b_n = (-1)^{n-1}\left[\frac{1.3.5...(2n-3)}{2.4.6...(2n-1)}\right], \tag{2.21 b}$$

and $f^2 = (\epsilon^2 - 1) < 1$. This convergence conditions requires that $\epsilon < \sqrt{2}$, which, from our discussion of (2.16) can always be fulfilled by making r large enough.

Using (2.14), (2.19) and (2.21 a, b) in (2.12), we find after some manipulation

$$\delta = 2Cr\sigma^{3/2}\xi^{1/2}(1 - \tfrac{4}{3}\xi) + O(\sigma^{5/2}). \tag{2.22}$$

Since $\sigma = (A/\alpha)r^{-3/4}$, the product $r\sigma^{3/2}$ yields a term in $r^{-1/8}$. When transposed, this provides the $\delta r^{1/8}$ scaling law discovered empirically. Henceforth, we shall call the quantity $r^{1/8}(2C)^{-1}A^{-3/2}\alpha^{3/2}$ the 'scale factor', and denote it by the letter G. Then (2.22) may be written*

$$\delta G \doteqdot \xi^{1/2}(1 - \tfrac{4}{3}\xi), \tag{2.23}$$

an expression which not only embodies the $r^{1/8}$ mapping law, but also exhibits the zero at $\xi = 0{\cdot}75$ already expected from the early investigation.

ξ	δG						$h(\xi)$
	$A = 2, \alpha = 2$			$A = 2, \alpha = 3$		$A = 1{\cdot}2$, $\alpha = 0{\cdot}7$	
	$r = 10$	$r = 50$	$r = 100$	$r = 50$	$r = 100$	$r = 50$	
0	0	0	0	0	0	0	0
0·1	0·280	0·276	0·275	0·276	0·275	0·290	0·274
0·2	0·335	0·329	0·329	0·330	—	0·348	0·328
0·3	0·336	0·331	0·330	0·330	0·329	0·349	0·329
0·4	0·303	0·298	0·296	0·298	0·299	0·314	0·295
0·5	0·244	0·239	0·237	0·238	0·237	0·251	0·236
0·6	0·164	0·157	0·156	0·157	0·156	0·168	0·155
0·7	0·066	0·059	0·058	0·058	0·057	0·065	0·056
0·8	−0·049	−0·056	−0·058	−0·058	−0·062	−0·056	−0·060
0·9	−0·177	−0·186	−0·188	−0·187	−0·190	−0·192	−0·190
1·0	−0·319	−0·329	−0·330	−0·330	−0·332	−0·340	−0·333

Table 2. Scaled fringe shift calculated from the exact form, equation (2.8), and from the approximate form, $h(\xi) = \xi^{1/2}(1 - \frac{4}{3}\xi)$; G = 'scale factor'.

We can get an idea of the amount of approximation involved in this equation by comparing values of δG calculated from the exact fringe-shift expression (2.8) with values of $h(\xi) = \xi^{1/2}(1 - \frac{4}{3}\xi)$. The comparison is made in table 2 for several combinations of r, A, and α. We notice that for constant A and α, the approximation improves as r increases; and for constant r, as the ratio A/α decreases. This is consistent with the fact that the approximate form $h(\xi)$ is obtained by neglecting powers of the term $\sigma = (A/\alpha)r^{-3/4}$.

* The authors are indebted to Dr Raymond Sedney for helpful discussions of the approximation procedure.

For $A/\alpha \leqslant 1$, the approximation is within 1% of the exact value for all traces with $r > 50$ diameters. For $A/\alpha = 1{\cdot}7$ and $r = 50$, the approximation is within 6% of the exact value.

Equation (2.23) shows that δG is constant along curves where $\xi = (x - x_N)/2Ar^{1/4} = \text{const.}$; or since

$$x_N = \alpha r + y_0 - Ar^{1/4},$$

along the lines

$$x = \alpha r + y_0 + Ar^{1/4}(2\xi - 1). \tag{2.24}$$

This family of curves, shown schematically as dotted lines in figure 8, includes the shock waves (when $\xi = 0$ and 1) and the straight characteristic $x = \alpha r + y_0$ (when $\xi = 0{\cdot}5$).

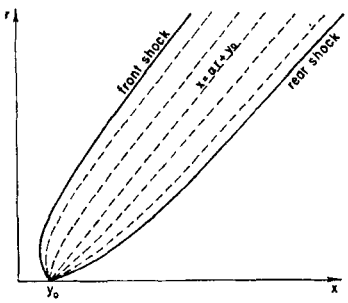

Figure 8. Lines of constant δG.

Equation (2.23) gives a convenient test for the existence of N-wave flow no matter what the Mach number. The fringe shift δ can be measured along a horizontal trace and multiplied by the scale factor. The existence of N-wave flow is established if this quantity, plotted against ξ, lies closely along the curve $h(\xi) = \xi^{1/2}(1 - \frac{4}{3}\xi)$.

2.6. *Application of theory to flow around blunt bodies*

Since all of the theory described above is based upon an N-wave pressure expression derived from slender-body theory, one would naturally select a slender projectile in any attempt to substantiate the theory experimentally. However, stability considerations, to be discussed later, make the slender projectile impractical and require that a sphere be used in the investigation.

From a theoretical standpoint it seems possible to use the disturbance from a sphere to verify the predicted N-wave fringe shift. Whitham (1950) shows that the pressure profile between the shocks far enough away from any supersonic body is linear, and that the pressure equation and the equation of the front shock take the form

$$p - p_0 = \gamma M^2 k^{-1}(2\alpha)^{-1/2} r^{-1}(x + h - \alpha r), \tag{2.29}$$

and

$$x = \alpha r - br^{1/4} - h, \tag{2.30}$$

respectively, where b and h are constants depending on body shape. These equations are of the same form as (2.2) and (2.3), which resulted from

slender-body theory. Although b and h depend upon the body shape, they are not explicitly set out in terms of body shape; whereas the constants A and y_0 of (2.2) and (2.3) are. We infer, therefore, as Lighthill (1954) has done, that equations (2.2) and (2.3) from Whitham's slender-body theory apply to the disturbance sufficiently far from the axis of any supersonic projectile, provided that the constants A and y_0 are evaluated empirically from the shock wave positions and other data.

3. Experimental procedure

3.1. *Theory of the experiments*

The experimental investigation is designed (1) to test the validity of the fringe-shift equation (2.8) between the shock waves, (2) to determine how near to the projectile axis the conditions characteristic of an ideal N-wave may be observed, and (3) to determine how near the axis the actual shock waves lie along the lines described by (2.2).

The first studies were made of the flow around a 0·225 in. cone-cylinder in a region about 15 projectile diameters from the axis (see first footnote of § 2.5). The fringe shift was much greater than that predicted for the ideal N-wave, and, in order to observe the flow further from the axis, it became necessary to use projectiles of smaller diameter. Final results were obtained with a $\frac{1}{16}$ in. diameter sphere, which permitted observations to be made at distances up to 70 diameters.

To substantiate the fringe-shift equation, the actual fringe shift is measured along a horizontal trace, multiplied by the scale factor, and compared with the function $h(\xi) = \xi^{1/2}(1-\frac{4}{3}\xi)$.

The scale factor is a function of C, α, and r; however, since the disturbance is caused by a blunt body, A cannot be calculated from the body shape, but must be determined from measurements of the shock wave positions with the help of the definition $A = (x_S - x_N)/2r^{1/4}$. The reliability of this method is tested by measuring the shock positions from a $\frac{1}{8}$ in. diameter sphere. Average values of A and y_0 are calculated from these positions and are used with (2.2) to plot the theoretical N-wave shock positions. These are compared with the measured positions.

From a theoretical point of view it would have been desirable to compare the measured shock positions of a projectile of known velocity and line of flight with the positions predicted by the shock equations (2.2). Actually it is impractical to determine the line of flight accurately in the free flight range. In order to fix the axis in an interferogram, the existence of the straight characteristic, $x = \alpha r + y_0$, lying halfway between the shocks, is assumed. The picture is adjusted until the slope of this line corresponds to the α calculated from velocity measurements. Our method for verifying the N-wave shock equations is thus a semi-empirical one.

3.2. *Apparatus and instrumentation*

To obtain quantitative data the projectiles were fired from a calibre 0·22 rifle approximately along the axis of the Controlled Temperature-Pressure Range of the Air Flow Branch, Exterior Ballistics Laboratory.

The flow was observed through optical glass windows at the interferometer station of the range by a Mach–Zehnder interferometer with an 8 in.× 10 in. working field. (For a detailed discussion of this type of instrument, see Ladenburg & Bershader 1954.)

In order to record the disturbance as far from the axis of the projectile as possible, the rifle was aimed to place the projectile near the edge of the interferogram. Fringes were adjusted to lie parallel to the trajectory.

The light source employed at the interferometer is an exploding wire with a duration of about 3 microseconds (Lewis & Sleator 1956). Since the projectiles travelled about 1·5 mm during this time, their images were stopped on the film with a rotating mirror (Bergdolt *et al.* 1951). A band of light about 20 Å wide centred at the 4358 Å mercury line is isolated from the continuous spectrum of the exploding wire by a slit and a carbon disulphide liquid-filled prism (Sleator *et al.* 1952).

The projectile velocity is measured between a pair of stations 16·89 ft. apart served by 0·1 megacycle chronograph counters triggered by impulses from photo-cells which respond to fluctuations in light screens through which the missile passes. The impulse from the down-range station also triggers a delay circuit, which fires the exploding wire of the interferometer station at the proper time.

The interferograms are measured with a Telereader–Telecordex combination. The Telereader projects a magnified image of the interferogram on a screen; horizontal and vertical cross hairs can be moved independently across the screen to measure distances in the r and x directions respectively. The distances moved by the cross hairs are displayed by the counters of the Telecordex and can be permanently recorded with an automatic typewriter. If the counters are zeroed when the cross hairs are at one point of the interferogram (for example, at the nose of the projectile), the coordinates of any other point are measured by moving the cross hairs to that point. The measurement is accurate to within two Telereader units.

3.3. *The slender cone-cylinder*

A cylinder of 0·225 in. diameter with a conical tip of 20° included angle was initially selected for this investigation. This projectile is stable in flight when fired with small initial yaw and high spin (cf. McShane *et al.* 1953), and it is just slender enough to meet the requirements of slender-body theory. A comparison of the results of Whitham's theory and the exact adiabatic theory of flow past a cone shows reasonably good agreement for included cone angles up to 20°.

The cylindrical portion of the projectile was made slightly oversize and was used as the rotating band in order to reduce the shock waves which attach themselves to the forward edge of a conventional rotating band. Even so, compression waves are propagated from the grooves engraved on the cylinder.

An interferogram (figure 9, plate 2) was taken of the flow around the projectile at a Mach number of 2·25. Fringe-shift measurements taken at

distances from the axis up to about 13 diameters indicated that the ideal N-wave had not formed within the field of view. The results of these measurements are reported in a later section only as a qualitative comparison with results obtained with spheres.

To observe the flow still farther away from the projectile axis, unsuccessful attempts were made to launch 0·1 in. diameter cone-cylinders. Sub-calibre projectiles such as these are made to fit the rifle bore by encasement in a plastic holder, called a sabot, which separates from the projectile after leaving the muzzle of the rifle. Difficulties arise because during separation the sabot imparts a certain amount of angular momentum and initial yaw to the projectile, and causes a body of borderline stability (such as the 20° cone-cylinder) to yaw violently or tumble in flight. It was therefore necessary to use a more stable projectile than the cone-cylinder. The sphere is a practical choice. It is stable, easily saboted, and can be readily obtained in almost any size.

3.4. *The spheres*

The spheres used were standard steel balls with diameters of $\frac{1}{8}$ in. and $\frac{1}{16}$ in. Since these were sub-calibre projectiles, sabots were necessary. The sabots were plastic cylinders 0·4 in. long and 0·225 in. in diameter whose forward faces were hollowed as inverted cones; the spheres were placed in shallow holes drilled at the apex of the cones.

An interferogram was taken of the flow around a $\frac{1}{8}$ in. diameter sphere (figure 10, plate 3) at a Mach number of 1·35. Shock-wave measurements from this interferogram are compared with the ideal N-wave shock equations (2.2) in § 4.2. Fringe-shift measurements, made at distances from the axis up to 40 diameters, indicated the need for a still smaller projectile.

Final firings were conducted with the $\frac{1}{16}$ in. sphere. The small size of this projectile presented two technical difficulties. (1) The muzzle velocity was somewhat unpredictable with the result that the delay set into the station circuits before a round was fired was not always compatible with the velocity attained. (2) The intensity of the light falling on the photocells at the velocity stations was frequently not influenced enough by the passing projectile to trigger the velocity counters. It was necessary, therefore, to fire many rounds to get two usable interferograms. For one of these interferograms the velocity of the round was measured, and the shock positions are clearly defined, but the quality of the fringes is too poor to allow accurate fringe-shift measurement. On the other hand, the fringes in the other are distinct and measurable, but the velocity was not obtained. No change was made in the inclination of the fringes nor in the gun position between the firing of these two rounds. Thus the inclination of the axis of flight with the fringes is presumably the same in both interferograms. Fringe-shift measurements are made on the interferogram shown in figure 11 (plate 4). The projectile axis is determined in conjunction with the interferogram for which the velocity is known.

4. Interferogram measurement and calculations

4.1. *Summary of the data*

Table 3 gives a summary of measured and calculated data. Items 1 to 8 list data measured in the laboratory at the time of firing. The air density, item 9, is determined from appropriate handbook tables using the measured values of temperature, pressure and humidity. The projectile velocity and Mach number, items 10 and 11, are calculated quantities; a discussion of velocity calculation for spheres is given in Appendix II. The quantity α is calculated from the Mach number for the projectile of figure 10 (plate 3); for the $\frac{1}{16}$ in. sphere of figure 11 (plate 4), α is the measured slope of the straight characteristic. The constants A and y_0, items 13 and 14, are calculated from shock-position measurements in a manner described in the next paragraph. To determine the undisturbed fringe spacing Δ, the distances between adjacent fringes are measured in the undisturbed region in front of the shock wave; Δ is an average of these measurements.

For those quantities which are used in a quantitative comparison with theory, table 3 gives the estimated error in the quantity. Where the datum is the average of a number of measurements or calculations (items 13, 14 and 15), the estimated error is given in the form of a standard deviation.

4.2. *Verification of the shock positions*

Before any measurements of the interferogram can be made, the picture must be oriented on the Telereader so that the origin of the coordinate system lies at the nose of the projectile and the x-axis along the axis of flight. Although this axis is not known, the velocity (and therefore α) has been measured. If the slope of the straight line running midway between the shocks is made to have the value α by adjusting the picture of the Telereader, then the x-axis of the Telereader will lie along the projectile axis.

The interferogram is initially placed in an arbitrary position on the Telereader. For some value of r, x_N and x_S are measured and x_0 calculated from $x_0 = \frac{1}{2}(x_S + x_N)$; for another value of r, another x_0 is determined in the same way. Now the coordinates of two points are known, and both points should lie on the line $x = \alpha r + y_0$ if the interferogram is properly oriented. Therefore, the slope of the line between the two points is calculated, and compared with the value of α calculated from the known velocity. If there is a discrepancy, the picture is rotated on the Telereader, and the same procedure is repeated. When the slope of the straight characteristic and α are as near to the same value as the Telereader adjustment will allow, then the x-axis is presumed to lie along the projectile axis.

Now the coordinates of the shock waves (x_N, r) and (x_S, r) are measured for many values of r. For each value of r we calculate (1) the point (x_0, r) on the straight characteristic from the relation $x_0 = \frac{1}{2}(x_N + x_S)$; (2) y_0 from

	0·255 in. Cone-Cylinder (figure 9, plate 2)	$\frac{1}{8}$ in. Sphere (figure 10, plate 3)	$\frac{1}{16}$ in. Sphere (not shown)	$\frac{1}{16}$ in. Sphere (figure 11, plate 4)
1. Temperature, T° C	24·5	24·5 ± 0·3	23·9 ± 0·3	23·9 ± 0·3
2. Barometric pressure, p_0 mm	769·6	768·8 ± 0·3	764·0 ± 0·3	758·4 ± 0·3
3. Humidity, %	33	38	43	43
4. Time of flight between stations, t microseconds	6523·0	9684·2 ± 0·1	7903·1 ± 0·1	Not measured
5. Distance between stations, z ft	16·879	16·714 ± 0·001	16·903 ± 0·001	Not measured
6. Diameter of projectile, d in.	0·225 0	0·125 0 ± 0·000 05	0·062 5 ± 0·000 05	0·062 5 ± 0·000 05
7. Mass of projectile, m gm		0·131 0 ± 0·000 05	0·017 0 ± 0·000 05	Not measured
8. Wavelength of light λ projectile diam. $\times 10^8$	7625·6	13·726 ± 94	27 452 ± 187	27 452 ± 187
9. Density of air, ρ_0 gm/litre	1·202 1	1·202 5 ± 0·003 4	1·194 7 ± 0·003 1	1·185 7 ± 0·002 7
10. Projectile velocity, V ft/sec	2562	1535 ± 69	1716 ± 77	Not measured
11. Mach number, M	2·258	1·353 ± 0·061	1·514 ± 0·071	Not measured
12. $\alpha = (M^2-1)^{1/2}$	2·024	0·911 ± 0·041	1·136 ± 0·051	0·810 ± 0·04
13. $\bar{A}$, (projectile diameters)$^{3/4}$	1·971	1·623	Not measured	1·663 ± 0·012
14. $\bar{y}_0$, projectile diameters	2·27	0·317	Not measured	Not measured
15. Undisturbed fringe spacing, Δ telereader units	65·96	Not measured	Not measured	60·2 ± 0·23
16. Scale factor/Δ, (telereader units)$^{-1}$	0·004 506 5	Not measured	Not measured	0·014 85 ± 0·000 23

$\lambda = 1{\cdot}405$; $K = 228{\cdot}81 \times 10^{-6}$ litre/gm.

Table 3. Summary of measured and calculated data.

$y_0 = x_0 - \alpha r$; (3) A from $A = (x_S - x_N)/2r^{1/4}$. We obtain an average $\bar{A}$ and $\bar{y}_0$. Through a plot of the points (x_0, r) a straight line is drawn, and the slope of this line is compared with α to make sure that any difference between them is less than the standard deviation of the α's found by taking numerous pairs of points from the set which determines the line.

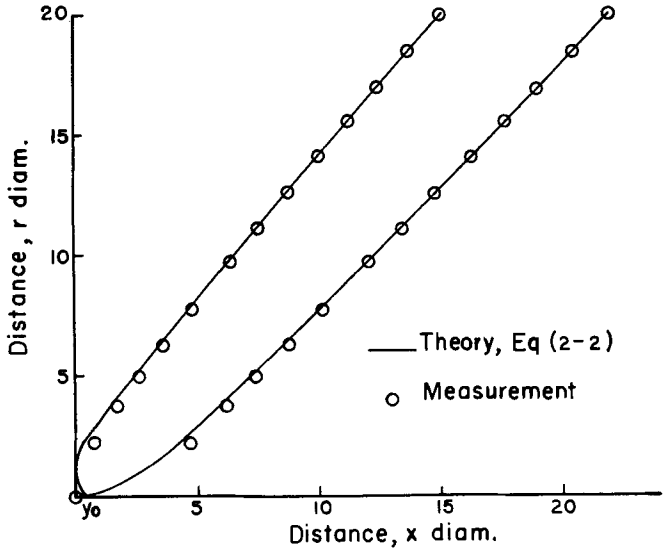

Figure 12. Shock positions, $\frac{1}{8}$ in. sphere.

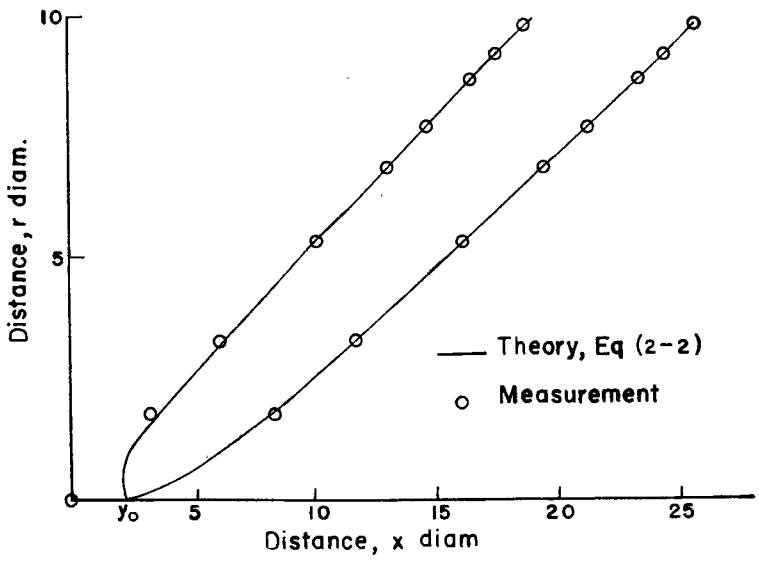

Figure 13. Shock positions, cone-cylinder.

Now the values $\bar{y}_0$, $\bar{A}$, and α are used in the shock equations

$$x_N = \alpha r + \bar{y}_0 - \bar{A} r^{1/4}, \qquad x_S = \alpha r + \bar{y}_0 + \bar{A} r^{1/4}.$$

For each value of r for which measurements were obtained, x_N and x_S are calculated. We compare calculated x_N, x_S with measured x_N, x_S for the $\frac{1}{8}$ in. sphere in table 4. Figures 12 and 13 show the measured and calculated shock positions for the sphere and the cone-cylinder respectively.

r	Measured x_N	Calculated x_N (N-wave)	Measured x_S	Calculated x_S (N-wave)
2·230	0·7831	0·364	4·721	4·332
3·676	1·719	1·416	6·222	5·912
4·916	2·610	2·377	7·451	7·211
6·276	3·666	3·463	8·789	8·601
7·711	4·829	4·634	10·203	10·044
9·626	6·385	6·223	12·041	11·941
11·062	7·527	7·430	13·433	13·350
12·552	8·789	8·691	14·793	14·803
14·053	10·029	9·971	16·239	16·257
15·532	11·225	11·237	17·686	17·683
16·925	12·411	12·436	18·991	19·022
18·415	13·694	13·723	20·460	20·449
19·948	15·010	15·051	21·928	21·913
21·384	16·316	16·298	23·233	23·280
22·874	17·621	17·596	24·626	24·696
24·723	19·154	19·218	26·355	26·458
26·214	20·481	20·514	27·802	27·860
28·030	22·167	22·106	29·629	29·576
29·520	23·407	23·414	30·999	30·982
31·141	24·854	24·839	32·555	32·509
32·707	26·246	26·218	34·034	33·982
34·350	27·562	27·666	35·503	35·526
35·851	29·020	28·991	36·938	36·935
37·014	30·010	30·018	38·015	38·026
38·135	30·934	31·009	39·146	39·077
39·821	32·522	32·500	40·767	40·656

Table 4. Comparison of N-wave shocks with actual shock positions for $\frac{1}{8}$ in. sphere. All units are in projectile diameters.

4.3. *Fringe-shift measurement, $\frac{1}{16}$ in. sphere*

The interferogram (figure 11, plate 4) is oriented on the Telereader so that the x-axis of the coordinate system is along the projectile axis and the shock positions are measured according to the procedure of § 4.2. The slope of the straight line through the points (x_0, r) is used to obtain α. Actually, the drag on the $\frac{1}{16}$ in. sphere is so great that the effective Mach number along the length of the shock waves is not constant, and three values of α are determined: one for the upper third of the shock wave region (this value, $\alpha = 0{\cdot}810$, is given in table 3), one for the middle third, $\alpha = 0{\cdot}800$, and one for the lower third where $\alpha = 0{\cdot}786$.

To interpret the interferogram the fringe shift δ is measured along the path traced by a fringe between the shock waves. If r is the radial distance to the disturbed fringe at a certain point (x, r) and r_u the distance to the same fringe in the undisturbed region in front of the shock, then $\delta = (r - r_u)/\Delta$, where Δ is the distance between the undisturbed fringes. The coordinates (x, r) along the fringe are measured for at least six values of x ranging from the front to the rear shock. For each value of x, six separate measurements are taken of the radial distance and averaged for r. Then δ is calculated at each point and multiplied by the scale factor.

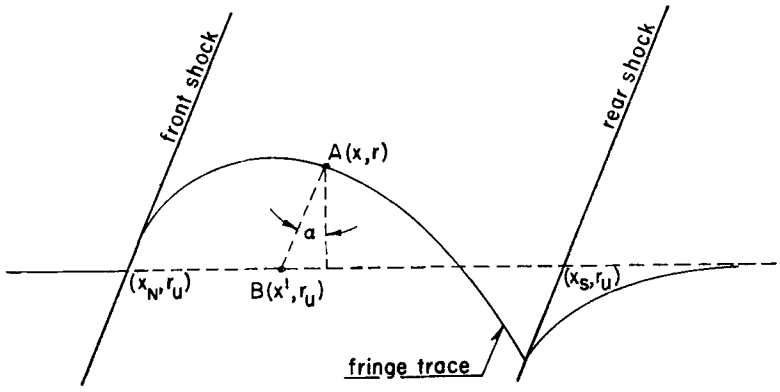

Figure 14. Correction of fringe-shift measurement.

The theory with which we wish to compare these measurements predicts fringe shift along a horizontal trace, not along a fringe; so we correct our measurements appropriately. It was shown in §2.5 that δG is constant along the lines

$$x = \alpha r + y_0 + A r^{1/4}(2\xi - 1).$$

The slope of these lines deviates from α by an amount that ranges from $Ar^{-3/4}$ at the shocks to zero midway between the shocks where $\xi = 0{\cdot}5$. For large r, $Ar^{-3/4}$ is small compared with α, and to a good approximation δG is constant along lines of slope α. We therefore move the measured δG at some point on the fringe, say $A(x, r)$ in figure 14, along a line of slope α to a new point, say $B(x', r_u)$, on the horizontal trace. By this construction, $x' = x - \alpha(r - r_u)$. The value of ξ corresponding to the δG measured at A is then $\xi = (x' - x_N)/(x_S - x_N)$. The change in $r^{1/8}$ of the scale factor due to the move from point A to point B is less than $0{\cdot}1\%$ for $r > 70$ diameters, and is neglected. Six separate measurements were taken of the distance between the shock waves $(x_S - x_N)$, and their average was used in the calculation of ξ. The value of A used in the scale factor is an average value determined from the shock wave positions in the manner described in §4.2.

The results of these fringe-shift measurements for several traces through the shock waves are given in figures 15 to 19, where δG is plotted against ξ and compared with the curve $h(\xi) = \xi^{1/2}(1 - \frac{4}{3}\xi)$.

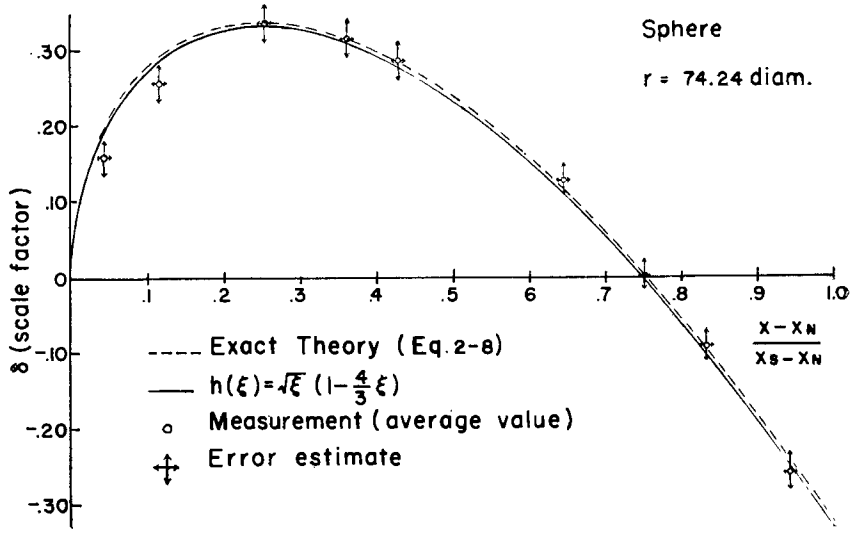

Figure 15. Fringe shift between the shocks.

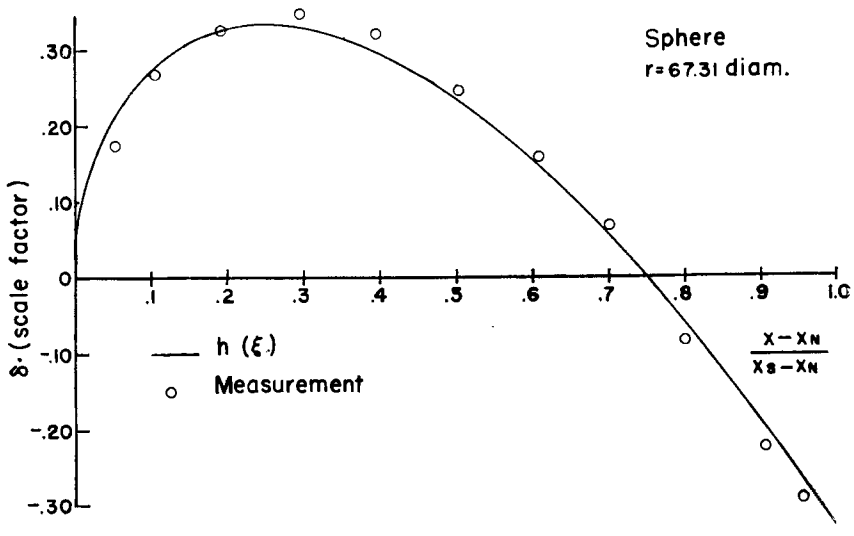

Figure 16. Fringe shift between the shocks.

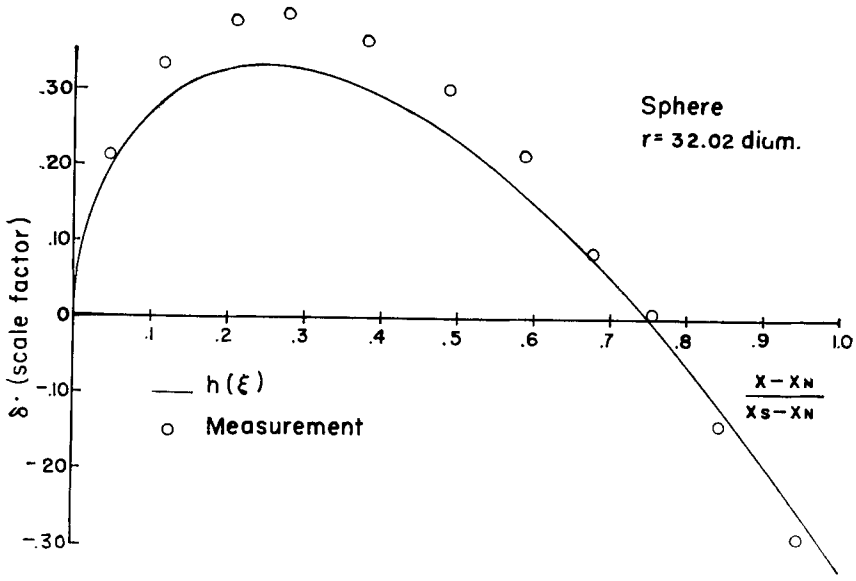

Figure 17. Fringe shift between the shocks.

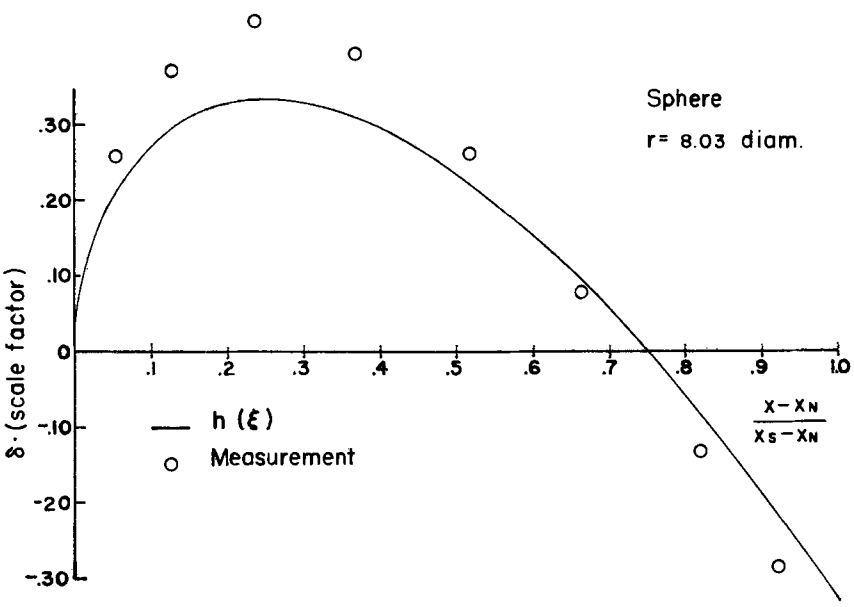

Figure 18. Fringe shift between the shocks.

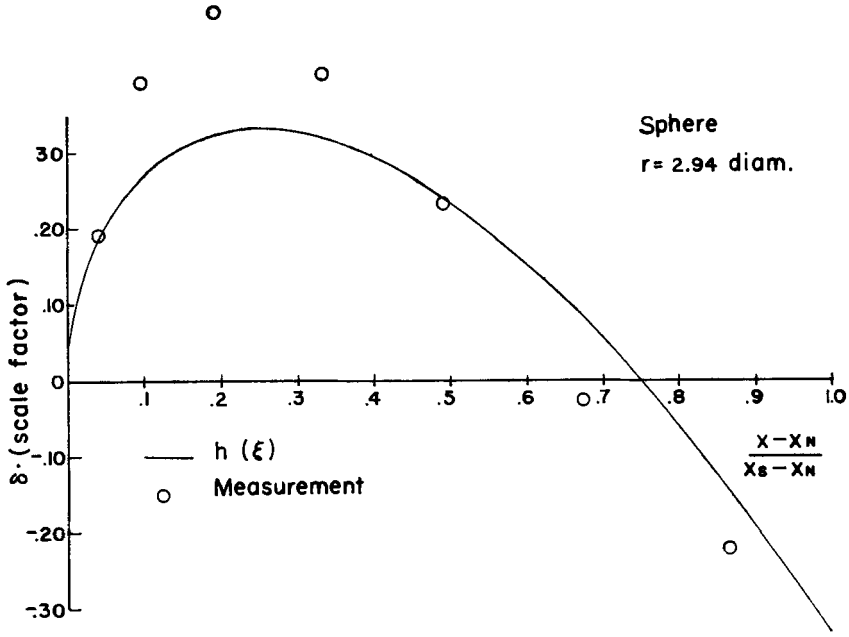

Figure 19. Fringe shift between the shocks.

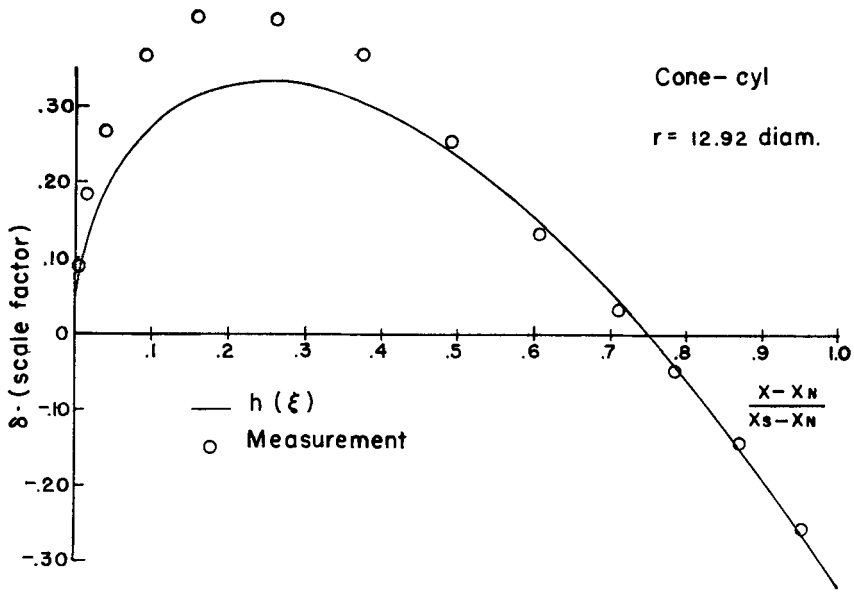

Figure 20. Fringe shift between the shocks.

4.4. *Fringe-shift measurements, cone-cylinder*

The interferogram of figure 9 (plate 2) was measured in the same manner as that of the sphere. The results are shown in figures 20 and 21.

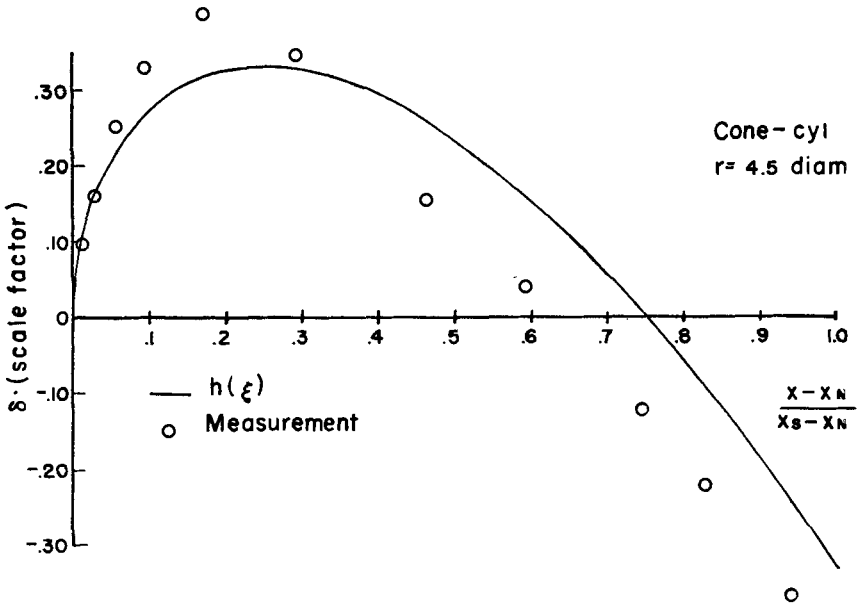

Figure 21. Fringe shift between the shocks.

5. Discussion of results and conclusions

5.1. *Shock positions*

Table 4 compares the actual shock positions for the $\frac{1}{8}$ in. sphere with the shock positions predicted for the N-wave by (2.2). Figure 12 presents this comparison pictorially. The calculated points plot a smooth curve, but the measured points have a randomness due to errors in the measurements. At small r, the measured points of the shocks fall well outside the N-wave curves of (2.2). For $r > 15$ diameters, the measured points fall randomly on either side of the N-wave curves and within $\frac{1}{10}$ of a diameter from them, which is estimated to be within the probable error of the measurements.

We assume the validity of (2.2) in order to determine the axis of the projectile and to measure the constants $\bar{A}$ and $\bar{y}_0$. We now conclude that this assumption is correct, and that the actual shock waves follow the curves given by (2.2) for all $r > 15$ diameters.

Whitham (1952) has interpreted the experimental results of DuMond *et al.* (1946) as showing that the shock waves follow the curves of (2.2) for $r > 1000$ diameters. The results given here indicate that good agreement is obtained closer to the projectile axis by a factor of 60.

A similar comparison of actual and N-wave shock positions for the slender cone-cylinder is shown in figure 13. For this projectile the curves coincide for $r > 7$ diameters.

5.2. *Fringe shift in the N-wave*

Figures 15 to 19 show the results of the fringe-shift measurements along several traces of constant r, and compare these results with the fringe shift predicted by the theory as represented by the curve $h(\xi) = \xi^{1/2}(1 - \frac{4}{3}\xi)$. For small r, the measured data lie well above $h(\xi)$ near the front shock and below $h(\xi)$ near the rear shock. We attribute this to the fact that in the near regions where the ideal N-wave has not yet formed, the pressure profile between the shocks lies above a linear profile near the front shock and below near the rear shock (see figure 3). As r increases, the measured fringe-shift curve moves closer to $h(\xi)$. At $r = 74$ diameters, the measured data fall very close to the exact theoretical curve of (2.8) (as represented by the dashed line of figure 15). The circles plotted in figure 15 are the average values of the measurements. The lengths of vertical arrows through these circles represent the composite estimated errors in the fringe-shift measurements and in the determination of the scale factor. The horizontal arrows show the estimated error in ξ. A detailed error estimate is given elsewhere (Steininger 1956).

We notice that for $r = 74$ and $r = 67$, in the region where fringe shift all along the trace is rather small, the data points just behind the front shock fall below the theoretical curve. In the *near* regions of both cone-cylinder and sphere within 10 to 15 diameters of the axis, the data points do not fall below the theory. However, in determining the value of ξ for each fringe-shift measurement (see §4.3), we moved the value of fringe shift down a line of slope α to the horizontal trace, whereas to be completely accurate we should have moved down a line of steeper slope. This means that a more accurate plotting of the data would move the points near the front shock wave to the right and hence below the theoretical curve. This correction would increase with increasing fringe shift since it is proportional to $r - r_u$, and with decreasing r since it is proportional to $Ar^{-3/4}$. An analysis of the errors involved in the measurements does not indicate the possibility of these low points. Therefore we must look for a physical basis for the discrepancy. A possible explanation is that refraction effects immediately behind the shock front displace the fringes slightly downward and result in a smaller fringe shift. Bennett *et al.* (1952) give evidence that fringe-shift data near the shock usually lie below expected values. More recent unpublished investigations indicate that refraction could cause measured values to lie either below or above expected values depending upon which side of the focal plane the projectile lies. The position of our projectile with respect to the focal plane is not known, so we cannot come to a definite conclusion about the effects of refraction in our particular case.

We conclude that (1) equation (2.8) does predict the fringe shift in the region between the shocks where the pressure profile is linear, (2) the approximate function $h(\xi) = \xi^{1/2}(1 - \frac{4}{3}\xi)$ can be used as a test for the

existence of N-wave flow, and (3) for the sphere, N-wave flow exists for r greater than about 70 diameters. We note in passing that the shock waves assume their asymptotic shapes much closer to the projectile axis than the pressure profile does.

The results of fringe-shift measurements for the cone-cylinder are presented in figures 20 and 21 for qualitative comparison with the results for the sphere. We see that as r increases, the peak value of the measured fringe shift moves away from the theoretical curve, giving evidence that the actual fringe shifts, and consequently the pressures in this region, are dissipating less rapidly than an N-wave pressure distribution which the theory represents. This is to be expected. Whitham (1952) shows that the pressure curve $Wh(71)$, if it applied at small r, would become infinite at $r = 0$, and that the shock strength at large r, $Wh(44)$, decreases at a rate proportional to $r^{-3/4}$. It seems reasonable that, in the case of the cone-cylinder where the conical region of compressive flow extends far up the front shock wave, the actual pressure, although having a finite value at $r = 0$, dissipates much less rapidly at small values of r than the N-wave pressure would.

In contrast, we notice that for the sphere where the flow is compressed at the front and then expands continuously around the body, the measured fringe shift converges upon the theoretical curve even in the relatively near regions.

Appendix I. Intersections of the functions f and Rg

From § 2.4,

$$f = (\epsilon^2 - 1)^{1/2} \tag{I.1}$$

and

$$g = \log[\epsilon + (\epsilon^2 - 1)^{1/2}]. \tag{I.2}$$

The functions f and Rg intersect when

$$(\epsilon^2 - 1)^{1/2} = R \log[\epsilon + (\epsilon^2 - 1)^{1/2}] \tag{I.3}$$

or

$$\exp[(\epsilon^2 - 1)^{1/2}/R] = \epsilon + (\epsilon^2 - 1)^{1/2}. \tag{I.4}$$

Let $\theta = (\epsilon^2 - 1)^{1/2}/R$. Then

$$e^{\theta} = \epsilon + (\epsilon^2 - 1)^{1/2}, \tag{I.5}$$

and

$$e^{-\theta} = [\epsilon + (\epsilon^2 - 1)^{1/2}]^{-1} = \epsilon - (\epsilon^2 - 1)^{1/2}. \tag{I.6}$$

Now

$$\sinh\theta = \frac{e^{\theta} - e^{-\theta}}{2} = (\epsilon^2 - 1)^{1/2}, \tag{I.7}$$

so

$$\sinh\theta = R\theta. \tag{I.8}$$

Figure 22 shows the relationship of the functions $\sinh\theta$ and $R\theta$. For the function $\sinh\theta$,

$$\frac{d}{d\theta}(\sinh\theta) \geqslant 1 \quad \text{for } \theta \geqslant 0.$$

For the function $R\theta$,

$$\frac{d(R\theta)}{d\theta} \leqslant 1 \quad \text{for } R \leqslant 1.$$

In these two cases, the only intersection of $R\theta$ with $\sinh\theta$ occurs at $\theta = 0$ ($\epsilon = 1$). When $R > 1$,

$$\frac{d(R\theta)}{d\theta} > 1,$$

and $R\theta$ and $\sinh\theta$ intersect twice, once at $\theta = 0$ and once for $\theta > 0$ ($\epsilon > 1$).

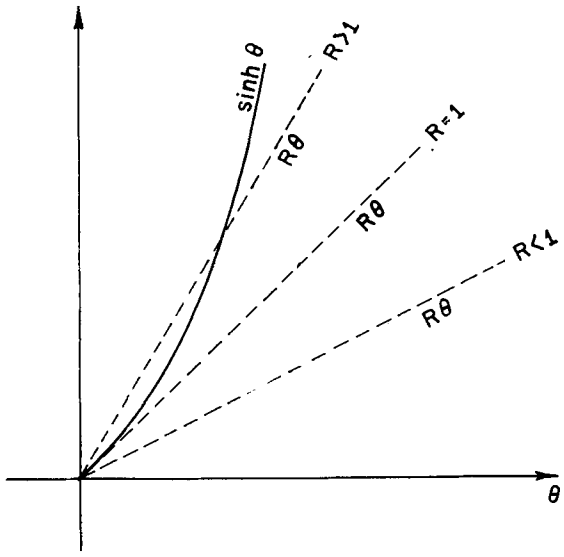

Figure 22. Relationship of the functions $\sinh\theta$ and $R\theta$.

Appendix II. Velocity calculation for spheres

The equation of motion for any non-yawing projectile in free flight can be written

$$\frac{dV}{dz} = -K_D F_0 V, \tag{II.1}$$

where V is the velocity of the projectile, and K_D the ballistic coefficient; also $F_0 = \rho_0 d^2/m$, where ρ_0 is the air density, d the diameter of the projectile, and m the mass of the projectile. From the work of Charters & Thomas (1945), for spheres,

$$K_D = (0{\cdot}3812 \pm 0{\cdot}0006) - (0{\cdot}0140 \pm 0{\cdot}0008)(V/c - 2{\cdot}75),$$

or in general terms

$$K_D = a(1 - bV), \tag{II.2}$$

where $a = 0{\cdot}4197$ and b is a constant which depends on the sound velocity.

Equation (II.1) now becomes

$$\frac{dV}{dz} = -F_0 aV(1 - bV), \tag{II.3}$$

which can be integrated to give

$$\frac{V}{1 - bV} = V_1 \exp(-F_0 az). \tag{II.4}$$

We replace V by dz/dt, integrate again and find that

$$\frac{\exp(F_0 az)}{F_0 a} + bV_1 z = V_1 t + C, \tag{II.5}$$

where C is the second constant of integration.

For the sphere shown in figure 10 (plate 3), the time t_1 required to traverse a distance z_1 between the two velocity stations of the range was measured. We evaluate the constant C in (II.5) from the initial condition that when $t = 0$, $z = 0$, and the constant V_1 from the final condition that when $t = t_1$, $z = z_1$.

Now the distance z_2 from the first velocity station to the interferometer is measured, and from (II.4) the value of V at the interferometer is determined thus

$$\frac{V}{1-bV} = V_1 \exp(-F_0 az_2). \tag{II.6}$$

References

Bennett, F. D., Carter, W. C. & Bergdolt, V. E. 1952 *J. Appl. Phys.* **23**, 453.

Bergdolt, V. E., Greenwald, A. J. & Sleator, D. B. 1951 A pressurized range for small caliber projectiles, *Aberdeen Proving Ground, BRLM Report* no. 548.

Bergdolt, V. E. 1953 *J. Aero. Sci.* **20**, 751.

Charters, A. C. & Thomas, R. N. 1945 *J. Aero. Sci.* **12**, 468.

Cole, J. D., Solomon, G. E. & Willmarth, W. W. 1953 *J. Aero. Sci.* **20**, 627.

DuMond, J. W., Cohen, E. R., Panofsky, W. K. H. & Deeds, E. 1946 *J. Acoust. Soc. Amer.* **18**, 97.

Giese, J. H., Bennett, F. D. & Bergdolt, V. E. 1950 *J. Appl. Phys.* **21**, 1226.

Giese, J. H. & Bergdolt, V. E. 1953 *J. Appl. Phys.* **24**, 1389.

Heaslet, M. A. & Lomax, H. 1954 *High Speed Aerodynamics and Jet Propulsion.* Vol. IX, Sec. D32, p. 330. Princeton University Press.

Karman, Th. von & Moore, N. B. 1932 *Trans. Amer. Soc. Mech. Engrs.* **54**, 303,

Ladenburg, R. & Bershader, D. 1954 *High Speed Aerodynamics and Jet Propulsion*, Vol. IX, Sec. A3. Princeton University Press.

Lewis, M. R. & Sleator, D. B. 1956 Exploding wire light source for high speed interferometry, *Aberdeen Proving Ground, BRLM Report* no. 975.

Lighthill, M. J. 1954 *High Speed Aerodynamics and Jet Propulsion*, Vol. IX, Sec. E6, p. 429. Princeton University Press.

McShane, E. J., Kelley, J. L. & Reno, F. V. 1953 *Exterior Ballistics.* University of Denver Press.

Sleator, D. B., Bergdolt, V. E. & Bennett, F. D. 1952 A monochromatic light source for interferometry of high speed gas flows, *Aberdeen Proving Ground, BRLM Report* no. 594.

Steininger, D. H. 1956 Interferometric analysis of the N-wave of a supersonic projectile. Dissertation, The Pennsylvania State University.

Whitham, G. B. 1950 *Proc. Roy. Soc.* A, **201**, 89.

Whitham, G. B. 1952 *Comm. Pure Appl. Math.* **5**, 301.